Controlling Excited-State Dynamics via Protonation of Naphthalene-Based Azo Dyes

Journal:	*Physical Chemistry Chemical Physics*
Manuscript ID	CP-ART-01-2024-000242.R1
Article Type:	Paper
Date Submitted by the Author:	01-Mar-2024
Complete List of Authors:	Martin, Shea; Lehigh University, Department of Chemisry Hamburger, Robert C; Lehigh University Huang, Tao; Lehigh University, Department of Chemisry Fredin, Lisa; Lehigh University, Lisa Fredin Young, Elizabeth; Lehigh University, Department of Chemistry

ARTICLE

Controlling Excited-State Dynamics via Protonation of Naphthalene-Based Azo Dyes

Shea M. Martin,[a] Robert C. Hamburger,[a] Tao Huang,[a] Lisa A. Fredin*[a] and Elizabeth R. Young*[a]

Received 00th January 20xx,
Accepted 00th January 20xx

DOI: 10.1039/x0xx00000x

Azo dyes are a class of photoactive dyes that constitute a major focus of chemical research due to their applications in numerous industrial functions. This work explores the impact of protonation on the photophysics of four naphthalene-based azo dyes. The pK_a value of the dyes increases proportionally with decreasing Hammett parameter of *p*-phenyl substituents from 8.1 (R = –H, σ=0) to 10.6 (R = –NMe2, σ= –0.83) in acetonitrile. Protonation of the dyes shuts down the steady-state photoisomerization observed in the unprotoated moieties. Fluorescence measurements reveal a lower quantum yield with more electron-donating *p*-phenyl substituents, with overall lower fluorescence quantum yields than the unprotonated dyes. Transient absorption spectroscopy reveals four excited-state lifetimes (< 1 ps, ~3ps, ~13 ps, and ~200 ps) exhibiting faster excited-state dynamics than observed in the unprotonated forms (for **1** – **3**: 0.7–1.5 ps, ~3–4 ps, 20–40 ps, 20-300 min; for **4**: 0.7 ps, 4.8 ps, 17.8 ps, 40 ps, 8 min) . Time-dependent density functional theory (TDDFT) elucidates the reason for the loss of isomerization in the protonated dyes, revealing a significant change in the lowest excited state potential energy nature and landscape upon protonation. Protonation impedes relaxation along the typical rotational and inversion isomerization axes, locking the dyes into a *trans*-configuration that rapidly decays back to the ground state.

Introduction

Azo dyes are intensely colored organic moieties that comprise one of the largest classes of dyes for textile coloring.[1] Azo dyes possess well-established photoswitching, *cis*/*trans* isomerization, and proton-transfer induced tautomerization that make them attractive for many applications including non-linear optical components,[2] optical data storage,[3] biological-medicinal studies,[4,5] and as materials for organic solar cells.[6] In particular, chemical control of photoisomerization has allowed azobenzene derivatives to be exploited as logic gates and for drug and small molecule release.[7–9]

The photophysics of azobenzene have been well studied as a model system for *trans* → *cis* photoisomerization. Most reports describe the photophysical evolution of azobenzene that begins with excitation into the symmetry allowed S_2 excited state. This S_2 excited state has an extremely short lifetime of ~0.1 ps that decays by rapid internal conversion to a vibrationally excited S_1 excited state.[10] The S_1 excited state cools in ~0.4 ps and undergoes internal conversion to a vibrationally excited ground state surface (S_0) in ~0.5-1.0 ps. This “hot” S_0 state is reported to have a vibrational cooling process with lifetimes of around 2 - 15 ps depending on solvent and whether it undergoes relaxation via a rotation or inversion mehcanism.[11] The light-driven *trans* to *cis* isomerization process in azobenzenes have been described by several molecular coordinates including rotation, inversion, concerted rotation and inversion-assisted rotation.[12] In many azobenzene systems, both in-plane inversion and out-of-plane rotations contribute to the isomerization processes, with the relative contributions of each mechanisms demonstrating sensitivity to the environment surrounding the azo dye.[11,13–25] The complex interplay between the shape of both ground state and excited state potential energy surfaces and where they cross, allows small chemical modifications to exert mechanistic control over the photoisomerization and reversion. [11,13–25]

Scheme 1. Protonated naphthalene-based azo dyes.

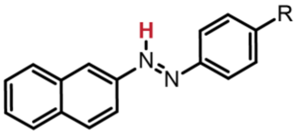

1 or 1H. R = H **2 or 2H**. R = OH
3 or 3H. R = OMe **4 or 4H**. R = NMe$_2$

---

[a] Department of Chemistry, Lehigh University, 6 E. Packer Ave., Bethlehem, PA 18015, USA.

Electronic Supplementary Information (ESI) available Synthetic details, ^{1}H NMR spectra, photoisomerization and reversion data, molar absorbtivities of **1**-**4**, transient absorption fitting analysis, DFT computed molecular orbital diagrams, relevant geometries of singlets, triplets and transitions states, potential energy surface, TDDFT energy tables, spin-orbit coupling constants. See DOI: 10.1039/x0xx00000x

Because the physical environment is critical to azo dye isomerization, the photoisomerization process can be controlled by exposure to specific solvents or steric constraints. Such efforts can be used to elucidate reaction mechanisms or control reaction pathways. For example, when azobenzene is encapsulated in a supramolecular organic capsule, bifurcation of the excited-state process occurs leading to a new excited-state inversion process that does not exist in solution.[26,27] Systematically changing the relative positions of azo bonds in bisazobenzenes (*o*- *m*- and *p*-connected) tune the initial photoexcited state and thus the light-induced dynamics. The *o*- and *p*-connected bisazobenzenes reduce the photoisomerization quantum yield due to intramolecular excitonic interactions or the extensive π-conjugation that enforces planarity, respectively. While, *m*-connected bisazobenzenes act as two independently behaving azobenzenes.[28] More substantial modification of the environments via addition of azobenzenes to larger side-chains or polymers further modifies or controls isomerization and photoswitching.[29–31]

Another means to control excited-state dynamics is through the introduction of protons. This strategy has been employed in inorganic complexes through the use of proton-sensitive ligands in rhenium(I) tricarbonyl diimine complexes with 1,4-pyrazine ligands,[32,33] with a 4,4'-biypridine ligand[34], and a 4-pyridylamidine ligand[35], among others. A few studies of photoisomerization of azo dyes in acidic environments have shown that at the switching timescales change[36–38] and that in some cased the photoisomerization mechanism can be effected.[39]

Indeed, proton-dependent ground-state properties of azo dyes have been reported using a host of electrochemical techniques resulting in the protonation or deprotonation of the azo/hydrazo bonds. Electrochemical reduction of azobenzene results in a stable anion radical in aprotic media that can become protonated.[40] The protonated species was more easily reduced a second time than the unprotonated counterpart.[41] A large positive shift in reduction potential was also observed when azobenzene was substituted with a pendant carboxylic acid functionality as a result of H-bonding.[42] These proton-dependent electrochemical properties extended to naphthalene-based azo dyes. The reduction potential of an anthracene-based azo dye recorded with organic acids spanning the pK_a range of 2.6–23.51 (in acetonitrile) revealed a linear dependence in the change of the reduction potential of the azo dye with the pK_a of the organic acid. A potential-pK_a diagram indicated a $1H^+/1e^-$ PCET process occurs in this window, allowing for the estimation of the pK_a of the azo dye to be 8.6 (in acetonitrile).[43]

Herein we report the influence of protonation on the photophysics of a series of four asymmetric naphthalene-based azo dyes (**1H** – **4H**, Scheme 1) through both experiment and density functional theory (DFT). The extended π-system afforded by the naphthalene moiety redshifts the UV-visible spectra of the dyes compared to azobenzene. The role of asymmetry in the rotation or inversion processes is examined. The electronic effects imparted by the increasing electron donating nature of the *p*-phenyl substituent is explored. UV-visible spectroscopy is used to observe the protonation of **1H** – **4H** and Benesi-Hildebrand analysis is used to quantify the acidity constant for each moiety. Increasing the electronic donating strength of the appended functionality increases the pK_a values of azo moiety (making them less acidic in acetonitrile). Photolysis experiments reveal that protonation of the azo dyes shuts down the observed bulk photoisomerization. Transient absorption spectroscopy is used to quantify the excited-state dynamics of **1H** – **4H**, which are compared to previous reported **1** – **4** analogues (Figure S1).[44]

Experimental

All reagents were obtained from commercial sources used as received without further purification, unless otherwise specified. Acetonitrile was dried over CaH_2 and distilled. Dried acetonitrile was stored over 4 Å molecular sieves. Dyes **1** – **4** were synthesized as described previously.[44] Protonation of dyes **1** – **4** to produce dyes **1H** – **4H** was carried out by addition of H_2SO_4 dissolved in acetonitrile (MeCN). Acid concentrations required to fully protonate each dye were determined via photometric titration as described below. All work in this manuscript is carried out in dried acetonitrile.

Instrumentation. Steady-state absorption spectra were collected using an Ocean Insight Flame UV-vis diode array spectrometer. A 1-ms integration time was used, and 100 scans were averaged for each collection. A boxcar width of 3 was used, which provides a spectral resolution of approximately 1 nm. Photoisomerization experiments were performed using a Luzchem LED Illuminator equipped with an LEDi-RGB illuminator head. Fluorescence spectra were obtained on an ISS Chronos BH fluorescence lifetime spectrometer with a steady-state upgrade.

Fluorescence Spectroscopy. Samples of **1H** – **4H** were prepared in acetonitrile to have less than 0.1 AU absorbance (in 1-cm pathlength) at the excitation wavelength. In order to minimize the internal filter effect, samples were excited along the 1 cm direction of the 1 cm × 0.2 cm cuvette and emission was measured from the 0.2 cm dimension. Each sample was subject to at least three freeze-pump-thaw cycles on a high-vacuum line to degas the samples (mTorr pressure in the cuvette). Samples were excited at 500 nm and emission was monitored from 520 nm to 800 nm. Sample 4H showed no emission and is omitted from emission spectroscopy results.

Photometric Titrations and Determination of Azo dye pK_a Values. Photometric titrations were conducted to ascertain the acidity constants of each azo dye beginning with a stock solution of dye **1**, **2**, **3** or **4** in acetonitrile and one stock solution of H_2SO_4 in acetonitrile. H_2SO_4 stock solution was prepared by dissolving 0.5 mL of concentrated H_2SO_4 in 10.0 mL MeCN and drying over 4 Å molecular sieves overnight to remove residual water. Two

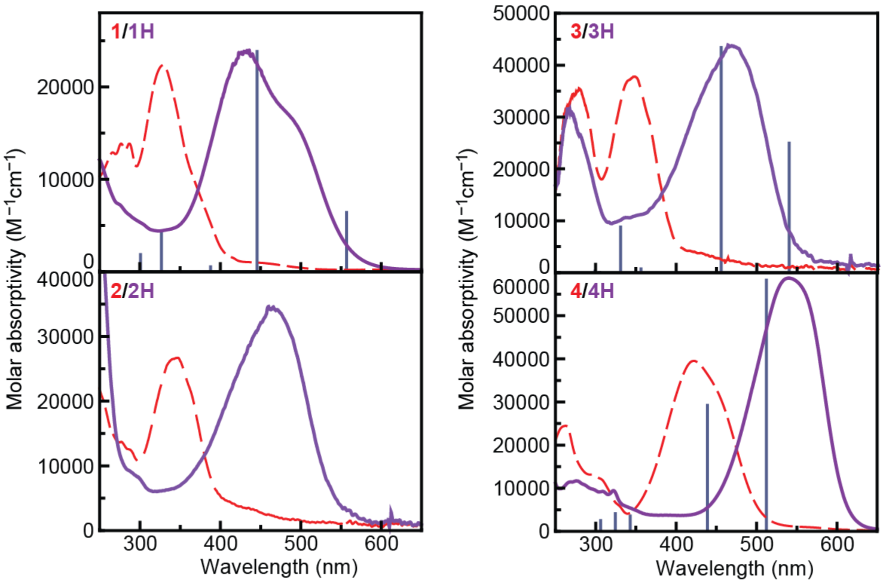

Figure 1. UV-visible absorption spectra of unprotonated **1** - **4** (red, dashed lines) in comparison to the protonated **1H** - **4H** (solid purple lines). Upon protonation, each azo dye demonstrates a red-shifted (>100 nm) and broadened absorption. TDDFT excitations for **1H**, **3H**, and **4H** are shown in blue overlaid with the experimental absorption spectra taken in MeCN and are normalized to the absorption maximum of the protonated spectra.

solutions, labeled A and B, were prepared for the titration by adding the same volume of the respective dye stock solution to two different 10.0 mL volumetric flasks to maintain the same concentration of dye in both solutions A and B. Solution A was finalized by filling the volumetric flask to the 10-mL line with dry acetonitrile. The concentrations of the azo dye (in Solutions A and B) were selected to give an absorbance of approximately 1 AU in a 1-cm cuvette. The stock solution of H_2SO_4 was added to solution B to achieve concentrations of H_2SO_4 at least double the amount needed to fully protonate the dye (1.4 × 104 mol equivalents acid for **1**, 2000 mol equivalents acid for **2**, 2000 mol equivalents acid for **3**, 30 mol equivalents acid for **4**). After addition of H_2SO_4 to the solution B flask, the volumetric flask was filled to the 10-mL line with dry acetonitrile. For the titration, solution B was titrated into a 2.0 mL portion of solution A in a quartz cuvette, beginning with a 1 uL addition. The addition volume of solution B was gradually increased as larger changes in the concentration of H_2SO_4 were required to achieve the same change in absorption. UV-visible absorption spectra of the resulting solution were collected after additions.

The titration data was plotted as $\frac{1}{\Delta A}$ vs $\frac{1}{[H_2SO_4]}$, where ΔA represents the change in absorption between solution A and the solution at a given H_2SO_4 concentration. The λ_{max} of the unprotonated or protonated species was used as the absorption wavelength for the analysis (λ_{obs} = 430 nm, **1**; λ_{obs} = 500 nm, **2** and **3**; λ_{obs} = 550 nm, **4**) as shown in Figure S3, with both wavelengths yielding similar results. The association constant K_{11} is obtained from the double reciprocal form of the Benesi-Hildebrand equation

$$\frac{\mathbf{b}}{\Delta \mathbf{A}} = \frac{1}{[\mathrm{S}]K_{11}\Delta\varepsilon[\mathrm{H_2SO_4}]} + \frac{1}{[\mathrm{S}]\Delta\varepsilon} \qquad (1)$$

where $\Delta\varepsilon$ is the change in molar absorptivity between the protonated and unprotonated species at the wavelength maximum of the protonated species, K_{11} is the experimental protonation constant, ΔA is the change in absorbance at the wavelength maximum of the protonated species and [H_2SO_4] is the concentration of acid used in these titrations. In this formalism, $K_{11} = \frac{\text{y-intercept}}{\text{slope}}$ of the linear fit to the data.[45] The pK_a values of dyes **1H** – **4H** were calculated by the relation

$$\mathbf{p}K_{\mathbf{a,azo\ dye}} = -\mathbf{log}\left(\frac{1}{K_{11}}\right) + \mathbf{p}K_{\mathbf{a,acid}} \qquad (2)$$

where the pK_a of H_2SO_4 in MeCN is 7.6.[46]

Photoisomerization. Samples of **1H** – **4H** were prepared in dry acetonitrile to an absorbance of ~1 AU at the absorption maximum (~ 0.1 mM). To measure the *trans* → *cis* conversion: The absorption spectrum of each sample was measured while under illumination from the LED lamp. The lamp head of the photoreactor was positioned directly above the samples in order to maximize exposure of sample to the incident light and the minimize scattering into the fiber optic lead of the diode array and. Three LEDs were used; UV (λ_{max} = 370 nm, fwhm = 12 nm, intensity = 155 mW), blue (λ_{max} = 453 nm, fwhm = 18 nm, 411 mW), and green (λ_{max} = 522 nm, fwhm = 30 nm, intensity = 143 mW). Samples of **1H** were illuminated using the UV and blue LEDs, samples of **2H** and **3H** were illuminated with UV, blue and green LEDs, and samples of **4H** were illuminated with blue and green LEDs in order to quantify the impact of illumination across the entire lowest energy absorption feature. Changes to the spectra of the dyes caused by exposure to light from the LEDs were found to revert rapidly when illumination ended.

Transient Absorption Spectroscopy. Transient absorption spectroscopy was performed with an Ultrafast Systems Helios spectrometer. Pulses (100-fs) of 800 nm laser light were

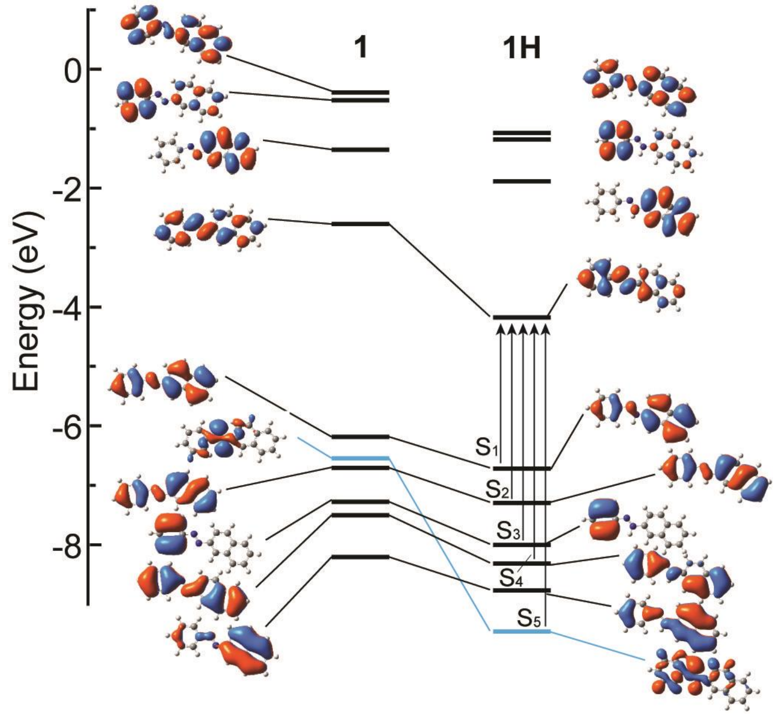

Figure 2. Frontier molecular orbitals of **1** and **1H**. The azo n-orbital is highlighted in blue and the first five singlet excitations are shown for **1H**, showing n-orbital is removed from the experimental window (λ_{ex} = 475 nm). B3LYP/6-311G(d.p)/PCM(ACN).

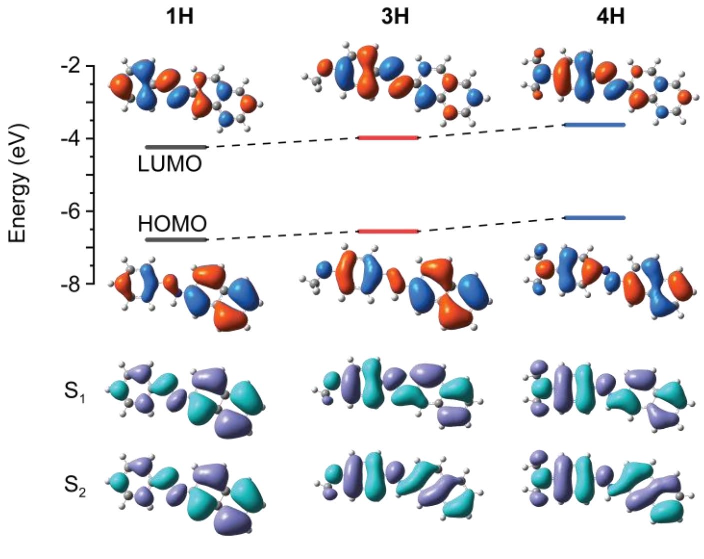

Figure 3. HOMO and LUMO orbitals for **1H**, **3H**, and **4H** and natural transition orbitals (NTO) of the S_1 and S_2 excited states. B3LYP/6-311G(d.p)/PCM(ACN).

generated with a Coherent Libra amplified Ti:sapphire system at 1.1 W and 1 kHz repetition rate. A beam splitter sends approximately 80% of the 800 nm pulse to a Topas-C optical parametric amplifier to generate the pump pulse (λ_{ex} = 370 nm), which was then converted to the desired excitation wavelength (475 nm for **1H**, 550 nm for **2H** and **3H**, 590 nm for **4H**). The remainder of each pulse (~20% of the 800 nm light) is sent through a CaF_2 crystal mounted on a translation stage to generate a white light continuum for use as the probe pulse. Excitation of the sample was carried out at ~ 0.1 mW to prevent decomposition of the sample.

The transient absorption spectra were measured over a 300-ps (**1H** – **3H**) or 5-ns (**4H**) window. For each scan, 250 time points were recorded and each sample was subjected to three scans. The sample was stirred with a magnetic stir bar during every run. Samples for transient absorption spectroscopy were prepared in on high vacuum line in a 2-mm quartz high-vacuum cuvette. An aliquot of the dye was introduced to the high-

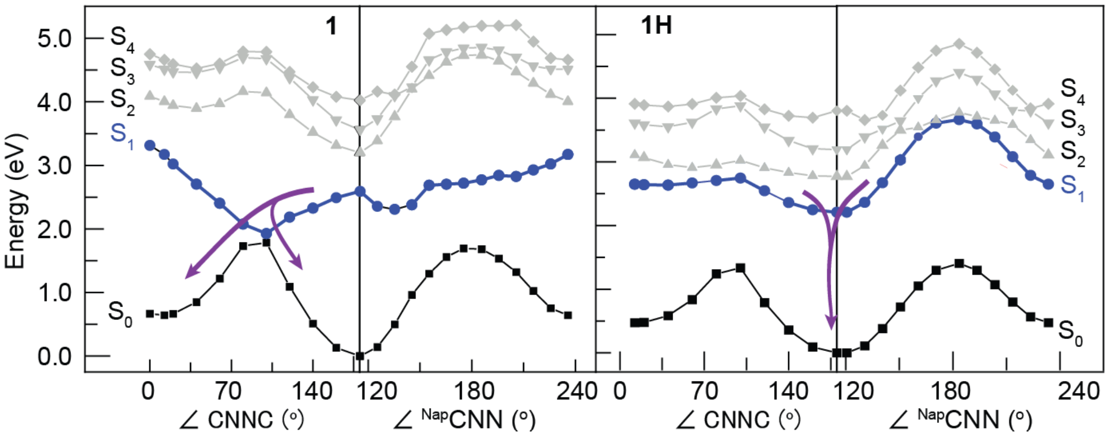

Figure 4. Comparison of the potential energy surfaces of **1** and **1H** along the torsional (∠CNNC) and inversion (∠^{Nap}CNN) *trans-cis* isomerization pathway. B3LYP/6-311G(d,p)/PCM(ACN). The S_1 PEC curve is emphasized with a bold, blue line (circle data points). Other singlet excited states are show in grey. Proposed excited-state pathways are shown in purple.

Table 1. Spectroscopic Data and Excited State Lifetimes of Protonated Azo Dyes

Dye	σ	Abs λ_{max} (ε $M^{-1}cm^{-1}$)	PL λ_{max}(nm)	PL QY	pK_a
1H	0	433 (23800)	550	1.9×10^{-2}	8.1 ± 0.4
2H	−0.37	494 (33500)	650	2.1×10^{-4}	9.4 ± 0.3
3H	−0.27	494 (43600)	610	7.9×10^{-4}	8.4 ±0.1
4H	−0.83	540 (58800)	n.a.	n.a	10.6 ± 0.2

vacuum cuvette and dried under vacuum. The cuvette was placed on the high vacuum line and solvent (~2 mL MeCN) was delivered through vacuum transfer. The concentration of each azo dye was ~30 µM. UV-visible absorption spectra were recorded before and after each TA experiment to verify that no decomposition had occurred.

Data preparation and cropping was done using Surface Xplorer data analysis software. A chirp correction (Figures S8, S10, S12, and S14) was applied during preparation of each data set. Data analysis was performed using single wavelength fitting and global analysis using our lab's Python-based analysis software (Figures S9, S11, S13 and S15) to isolate decay-associated difference spectra (DADS) and their corresponding lifetimes. Quality of the fitting was assessed by examining the residuals of principle component kinetic traces and the model used to represent the dataset.

Quantum Mechanical Calculations. Density functional theory (DFT) and time-dependent density functional theory (TDDFT) were performed on dyes **1H**, **3H** and **4H**. Dye **2H** was omitted to reduce computational cost as the experimental results of **2** and **3**, and **2H** and **3H** are similar to each other.[44] All calculations were run in Gaussian09[47] with a hybrid functional, B3LYP,[48–51] and triple-ζ basis set, 6-311G(d,p),[52–56] with a complete polarized continuum model (PCM) of acetonitrile. The fully optimized structure for each molecule was confirmed as a true minimum with no imaginary frequencies. The lowest energy protonation location of **1H**, **3H** and **4H** were confirmed by fully optimizing each dye with protonation at either the nitrogen adjacent to the naphthalene and to the phenyl. For **4H**, an additional possible protonation at the nitrogen on the dimethylamine moiety was tested and found to be less stable than protonation at either nitrogen on the azo bond (Figure S16). In all three cases, protonation at the nitrogen adjacent to the naphthalene was found to be the most stable protonation site.

The lowest energy singlet (S_0) surfaces (Figures S20-21) of **1H**, **3H** and **4H** were constructed through a relaxed scan of the CNNC dihedral angle and the CNN angle on both the naphthalene (∠^{Nap}CNN) and phenyl (∠^{Ph}CNN) sides of the azo bond in increments of 10-15°, where only the designated angle is constrained and all other coordinates are freely optimized. Excited-state potential energy curves were created by calculating the first 6 vertical singlet and triplet excitations at each point along the relaxed rotational and lowest inversional (i.e. ∠^{Nap}CNN or ∠^{Ph}CNN) ground-state curves.

Results and discussion

Protonation of azo dyes 1 – 4 to make 1H – 4H. The lowest energy protonation location of **1H**, **3H** and **4H** was determined

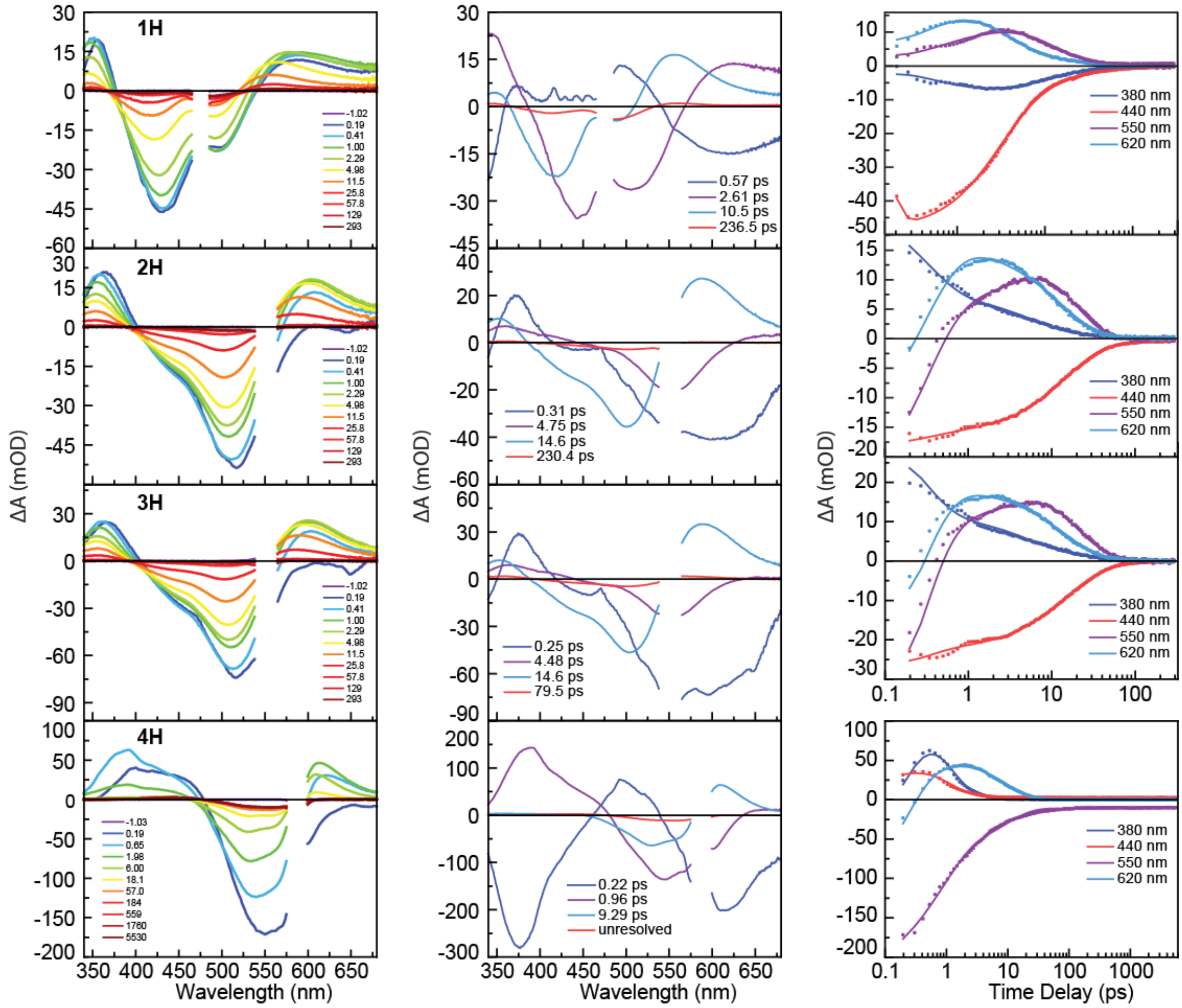

Figure 5. Representative spectra (left), decay-associated difference spectra (DADS) (center), and single-wavelength fits (right) of **1H** – **4H** for TAS data collected at λ_{ex}(**1H**) = 475 nm, λ_{ex}(**2H**) = λ_{ex}(**3H**) = 550 nm and λ_{ex}(**4H**) = 590 nm. Samples were prepared under a nitrogen environment in a 2-mm quartz high-vacuum cuvette in MeCN. DADS from global analysis fitting of azo **1H** – **4H** with associated lifetimes next to each spectrum for the individual run shown. The lifetimes obtained for this specific set of data are shown in the figure, and the average of multiple runs are reported in Table 2. For **4H**, τ_4 was too long to be observable on TAS timescales, but was resolvable on nanosecond TAS.

to be the nitrogen adjacent to the naphthalene (Figure S16 and S17). The computed energies for **1H** protonated on either the naphthalene-adjacent or phenyl-adjacent nitrogen are nearly isoenergetic, indicating a mixture of the two species. The predicted absorption spectra of the two protonation states are very similar (Figure S17) so the naphthalene-adjacent structure, which is the lower energy, is used going forward for simplicity. Titration of H_2SO_4 into solutions of **1** – **4** shows clean conversion of unprotonated **1** – **4** to protonated **1H** – **4H** with well-anchored isosbestic points (Figure S3). The protonation titration was analyzed using a Benesi-Hildbrand analysis (Eq. 1)[45] to yield an association constant (K_{11}) that represents the interaction between the azo dyes and the H_2SO_4. Using K_{11} and the relationship described in Eq (2), the pK_a values for each azo dye can be determined (Table 2). The pK_a value was plotted as a function of the Hammett parameter for each *p*-phenyl –R group to reveal a linear relationship between the pK_a and the Hammett parameter (σ) (Figure S4)[57]. As the electron donating strength of the functionality is increased from **1H** (σ = 0) to **4H** (σ = –0.83) the acidity constant increases from pK_a = 8.1 to pK_a = 10.6. This trend confirms that increasing electron donation *para* to the azo bond does increase the electron density on the N=N, causing it to require less acid to protonate.

Steady-state spectroscopy of protonated azo dyes. UV-visible absorption spectra and photoluminescence (PL) spectra of **1H** – **4H** in acetonitrile (Figure S2 and summarized in Table 1) show a redshift of more than 100 nm (Figure 1) upon protonation. In addition to a redshift, the spectrum of **1H** (Figure 1 purple solid line) is broadened compared to the spectrum of **1** (Figure 1 red dotted line). Both the redshift and peak intensities of **1H**, **3H** and **4H** are well-captured by TDDFT (Figure 1, blue vertical lines). The lowest-energy absorption feature of **1H** shows contribution from two states (λ_{max} = 488 nm and a clear, red-shifted shoulder) as predicted by TDDFT for either protonation at naphthalene-adjacent or phenyl-adjacent nitrogen. TDDFT also predicts two low-energy transitions for both **3H** and **4H**, however these transitions are closer in energy than those predicted for **1H**. In the experimental absorption spectra of both **3H** (λ_{max} = 494 nm) and **4H** (λ_{max} = 540 nm), a clear maximum is observed, however, a slight shoulder is observable to the blue of each λ_{max}. This shoulder is indicative of another band in accordance with the TDDFT results.

As the electron withdrawing strength of the *p*-phenyl substituent is increased, the absorption maximum of the azo dye redshifts with **2H** and **3H** showing nearly coincident absorption spectra in acetonitrile. The LUMOs of the protonated dyes are stabilized by ~ 1.7 eV driving the significant redshift observed in the absorption spectra. The absorption of the protonated dyes is dominated by the allowed transitions between the first 5 frontier orbitals (predicted at ~561 nm, ~447 nm and ~388 nm in **1H**) (Tables S2 – S4). The HOMO (Figure S18) of each dye is stabilized slightly upon protonation. The most critical change to the electronic structure compared to the unprotonated **1** – **4** moieties is stabilization of the non-bonding n-orbital by over 2 eV upon protonation. This effectively removes the symmetry unallowed excitations from the n-orbital from the low energy excitation manifold (Figure 2 and Figure 3) and drives the significant red-shift of the absorptions spectrum.

PL spectra were recorded for excitation at the λ_{max} of each azo dye. PL spectra were recorded for **1H** – **3H** that redshifted with the shifting absorption spectra. No PL was detected for **4H**, which is unsurprising as the unprotonated **4** is nonemissive.[44] Quantum yield values for **1H** – **3H** range from 0.02% to 2%. These quantum yields are significantly lower than those of the unprotonated **1** – **3** and decrease with the Hammett parameter of the *p*-phenyl substituent. This behavior indicates that increasingly electron-donating substituents on the periphery of the dye increases the likelihood for the dyes to deactivate *via* nonradiative pathways.

Photoisomerization of azos 1H – 4H. Photoisomerization experiments were carried out using a photolysis lamp with three different LEDs that allowed for excitation in to the S_2 absorption peak for the four azo dye moieties (LED λ_{max} = 370,

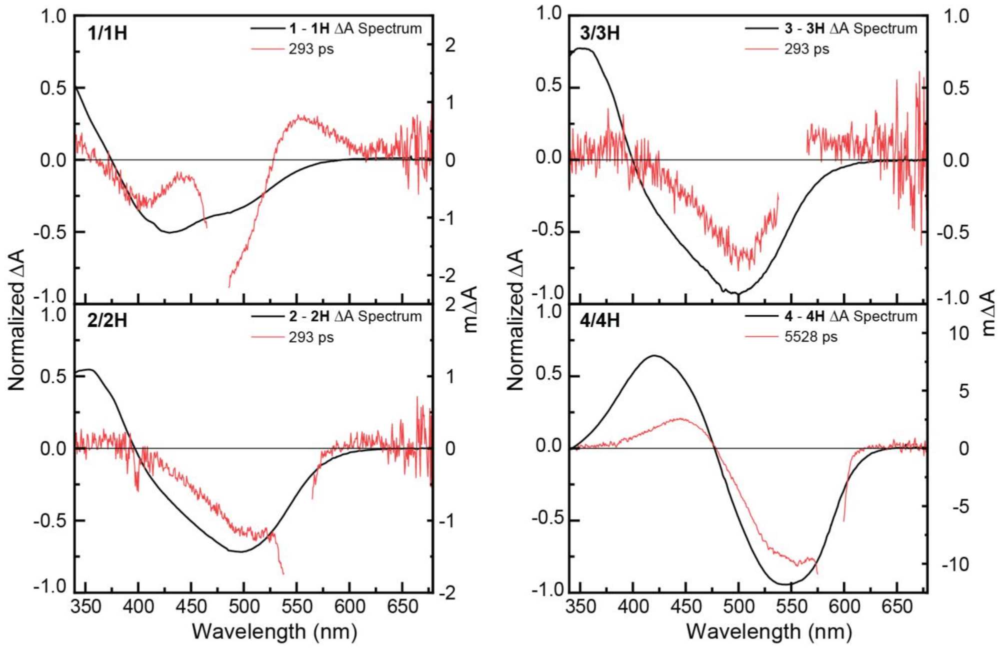

Figure 6. Difference spectrum of the protonated and unprotonated **1** – **4** compared to the last representative spectrum of their respective TAS data.

Table 2. TAS Lifetimes of Protonated Azo Dyes

	τ_1 (ps)[a]	τ_2 (ps)[a]	τ_3 (ps)[a]	τ_4 (ps)[a]
1H	0.68 (0.14)	2.5 (0.2)	9.9 (1.0)	230 (30)
2H	0.27 (0.03)	3.9 (0.7)	14.4 (0.19)	330 (80)
3H	0.25 (0.03)	3.8 (0.7)	14.7 (0.5)	90 (15)
4H	0.20 (0.02)	0.95 (0.02)	8.1 (1.1)	Unresolved

[a] *The lifetimes (and standard deviations) are the average of multiple datasets.*

453 nm and 522 nm). As reported previously, the unprotonated **1** – **4** azo dyes readily undergo photoisomerization, as indicated by a significant decrease in the absorption spectra of the *trans*-isomers of the dyes with a simultaneous growth of features representing their *cis* isomers (shown in Figure S5).[44] After protonation to form **1H** – **4H**, however, excitation into the primary absorption features does not yield any change to their overall absorbance spectra (Figure S5). This observation indicates that upon protonation, the bulk photoisomerization of **1H** – **4H** is shut down entirely.

Potential energy curves (PECs) of the singlet excited-state manifold (Figure 4) as well as the triplet-excited state manifolds (Figures S19 – S21) of **1H**, **3H**, and **4H** were constructed to rationalize their lack of photoisomerization. All dyes show similar ground- and excited-state PECs.

In contrast to the unprotonated **1**, the S_1 surface of **1H** is much flatter along the rotational axis and significantly uphill in energy (bolded blue first singlet excited state, S_1) upon inversion (Figure 4). Both isomerization coordinates of **1H** have S_1 minima at the *trans* configuration. Thus, the computed PECs show that the protonated azo dye is essentially locked into the Frank-Condon state (*i.e. trans*-configuration) and thus deactivates in the *trans* configuration rather than undergoing isomerization unlike the unprotonated dyes.

Ultrafast photoevolution of azo dyes 1H – 4H. Transient absorption (TA) spectroscopy was performed on each dye to quantify the excited-state dynamics of each moiety. **1H** was excited at 475 nm, **2H** and **3H** were excited at 550 nm and **4H** was excited at 590 nm. Figure 5 (left column) shows the TA spectral evolution over ~300 ps (**1H** – **3H**) or ~5 ns (**4H**). The transient signals of azo **1H** – **4H** each exhibit broad induced absorption features (at ~350 nm and 600 nm) in our spectral window of 350 nm to 675 nm that are convoluted with their respective ground-state bleach features (~ 425 nm (**1H**), 525 nm (**2H**, **3H**) ~550 nm (**4H**)). Over the first several picoseconds, the representative spectra show a blue-shift of the positive features on either side of the ground-state bleach that is typically ascribed to a vibrational cooling process. The transient signals for **1H** – **4H** then each return to the baseline over the course of the 300 ps or 5.5 ns TAS window.

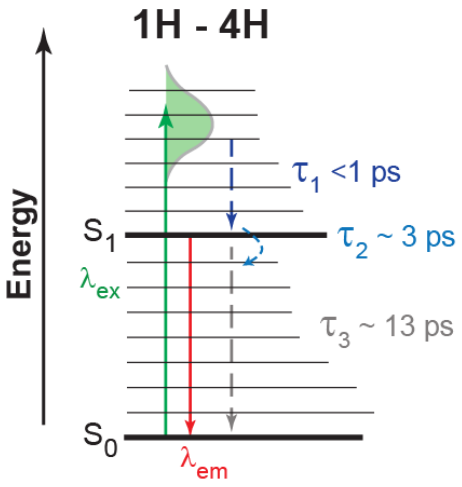

Figure 7. Jablonski diagram showing proposed relaxation scheme of **1H** – **4H**. λ_{ex}(**1H**) = 475 nm, λ_{ex}(**2H**) = λ_{ex}(**3H**) = 550 nm, λ_{ex}(**4H**) = 590 nm. Solid lines indicate radiative processes and dashed lines indicate non-radiative processes. The lifetime for the emission process was not resolved in our measurement due to low yields.

Global lifetime analysis (GLA) fitting of the TAS data yields a best fit to four lifetimes and produces four decay-associated difference spectra (DADS) associated with each of the four lifetimes (Figure 5 (middle column) and summarized in Table 2). The first component (τ_1) fits to lifetimes of 0.22 – 0.57 ps for azo **1H** – **4H**, while the second component (τ_2) has slightly longer lifetimes of 0.96 – 4.75 ps and the third component (τ_3) has a lifetime of 10 – 15 ps. The fits of **1H** – **3H** yield a fourth, low-contribution, longer-lived component (τ_4) with lifetimes ranging between 80 – 240 ps. For **4H**, GLA produces a fourth, low-contribution, long-lived component (τ_4) the lifetime of which is too long to be resolved on our 5-ns TAS detection window. The lifetimes determined by GLA fitting, when represented as single wavelength decay traces represent the data well across the entire spectral window for each of the azo moieties **1H** – **4H** (Figure 5 (right column), and Figures S9, S11, S13 and S15).

A photophysical mechanism for the excited-state decay of **1H** – **4H** (Figure 7) is constructed based on literature precedent[58–60], including our previous work [44] on unprotonated **1** – **4** (summarized in Table S1 and Figure S1), and is informed by (1) our steady-state observation of no bulk *cis*-isomer formation and (2) the computed TDDFT PECs, which show no driving force for inversion or rotation towards a *cis*-isomer. Based on these factors, we propose an excited-state mechanism in which **1H** – **4H** remain in their initial Franck-Condon (*trans*-isomer) state and undergo only vertical transitions between the various excited states. Excitation occurs directly into the S_1 state for each **1H – 4H** (Tables S2 – S4). TDDFT predicts two low-energy transitions that could potentially be populated with this initial excitation. Both of these S_1 and S_2 states are $\pi\pi^*$ transitions that initiate from slightly different symmetries on the naphthalene moiety (Figure 2 and Figure 3). The IC between these two similar states is expected to be faster than the time resolution of our instrument and thus the dynamics start from the lowest-energy S_1 state. The shortest component we observe (τ_1) for **1H** – **4H** therefore represents the cooling of the vibrationally-hot S_1 state. The τ_2 lifetime component represents the internal conversion of the S_1 state to a vibrationally hot S_0 ground state. Because of the lack of driving force for isomerization in the S_1 excited states, this hot S_0 is predicted to within 5-10° of the Franck-Condon state (*trans*-isomer). Thus, the τ_3 component represents cooling of the vibrationally hot S_0 to the fully relaxed ground state. These three lifetime are shorter than the lifetimes reported for the corresponding processes in the unprotonated species (for **1** – **3**: τ_1 =0.7–1.5 ps, τ_2 = ~3–4 ps, τ_3 = 20–40 ps; for **4**: τ_1 = 0.7 ps, τ_2 = 4.8 ps, τ_3 = 17.8 ps), and are consistent with the ultrafast dynamics previously observed for similar systems on short timescales. [58–60]

Our GLA model produced a fourth, low-contribution (<5%), long-lived component (τ_4) that does not fit with the described mechanism of rapid vertical transitions between the excited states. This signal was quite low, making it difficult to assign and adding uncertainty to the fitted lifetime. The low magnitude indicates that this process is a minor contribution to the photophysical evolution resulting from an off-path process. The fourth lifetimes do not correlate to the Hammett parameter of the *p*-phenyl substituent as other isomerization-related lifetimes for **1** – **4** or **1H** – **4H**. The difference absorption spectrum representing the unprotonated-protonated spectrum for each dye compared to the TAS representative spectrum at the longest times measured (~290 ps for **1H** – **3H**, and ~5500 ps for **4H**) (Figure 6) reveal similar spectral structure in each dye. We therefore propose that the fourth, off-path component represents a small residual signal from photo-deprotonation of the dyes, which re-protonates over the course of 10's of ps (or longer in **4H)**.

Conclusions

This study contributes experimental and computational results describing and rationalizing the photoisomerization, lifetime dynamics, quantum yields, and spectral characteristics of a series of protonated azo dyes. The UV-visible absorption maximum and corresponding photoluminescence (PL) spectra of **1H** – **4H** in acetonitrile redshift with increasing electron-withdrawing strength of the phenyl substituent. Similarly, the pK_a value of each dye increases with the increasing electron donating strength of the *p*-phenyl substituent. This shift is caused by increasing electron density on the naphthalene-adjacent site on the azo bond. PL spectra shifted along with absorption spectra for **1H** – **3H**. The calculated fluorescence quantum yields for **1H** – **3H** ranged from 0.02% to 2%, decreasing with the increasing electron-donating strength of substituents on the phenyl ring. These values are significantly lower than those of their unprotonated counterparts, meaning the likelihood of deactivation via nonradiative pathways increases in the protonated moieties.

A significant difference in the *trans* – *cis* photoisomerization behavior for protonated **1H** – **4H** was observed compared to the unprotonated azo dyes **1** – **4** that readily undergo photoisomerization. [44] For **1H** – **4H**, photoisomerization that is observed in **1** – **4** is entirely shut down. Transient absorption spectroscopy and global analysis fitting uncovers three excited-state lifetimes that can be ascribed to relaxation within the excited-state manifold at the Franck-Condon state (the *trans*-isomer configuration). These dynamics are more rapid than those of **1** – **4**. Computational insight provided by DFT and TDDFT show that the excited-state potential energy curves along the isomerization coordinates (rotational or inversion angles for azo bond) of **1H** – **4H** are uphill in energy, essentially forcing the excited state of the dye to remain in the *trans*-configuration. The corresponding curves of **1** – **4** are downhill, thereby moving the excited state evolution of the unprotonated species away from the Franck-Condon state towards the *cis*-isomer configuration. Therefore, the lack of photoisomerization in **1H** – **4H** is attributed solely to shutting down production of the *cis*-isomer. These findings provide valuable insights into the intricate photophysics of these molecules by rationalizing how the protonation of these dyes controls the photoisomerization process.

Author Contributions

Shea Martin: Investigation (equal), Formal analysis, Writing – original draft; Robert Hamburger: Investigation (equal), Formal analysis; Tao Huang: Investigation (equal), Formal analysis; Lisa Fredin: Conceptualization, Supervision, Writing – review & editing; Elizabeth Young: Conceptualization, Supervision, Writing – original draft.

Conflicts of interest

There are no conflicts to declare.

Acknowledgements

The authors thank the NSF Major Research Instrumentation program (CHE-1428633) for funding that established the laser facility. Acknowledgment is made to the Donors of the American Chemical Society Petroleum Research Fund for partial support of this research (PRF #65343-ND6). This work made use of the Lehigh University NMR Facility. The Bruker Neo 500 MHz NMR was acquired through NSF-MRI-1725883, with additional support from Lehigh University. Portions of this research were conducted with research computing resources provided by Lehigh University and the TG-CHE190011 allocation from Extreme Science and Engineering Discovery Environment (XSEDE), which is supported by National Science Foundation grant number ACI-1548562. Financial support for this research comes from Lehigh University.

References

1 A. Bafana, S. S. Devi and T. Chakrabarti, *Environmental Reviews*, 2011, **19**, 350–370.
2 S. K. Yesodha, C. K. Sadashiva Pillai and N. Tsutsumi, *Prog Polym Sci*, 2004, 29, 45–74.
3 H. Mustroph, M. Stollenwerk and V. Bressau, *Angewandte Chemie International Edition*, 2006, **45**, 2016–2035.
4 Y. Ali, S. A. Hamid and U. Rashid, *Mini-Reviews in Medicinal Chemistry*, 2018, **18**, 1548–1558.
5 V. M. Dembitsky, T. A. Gloriozova and V. V Poroikov, *Nat Prod Bioprospect*, 2017, **7**, 151–169.
6 L. Zhang and J. M. Cole, *ACS Appl Mater Interfaces*, 2014, **6**, 3742–3749.
7 W. Chen, C. A. Cheng, D. Xiang and J. I. Zink, *Nanoscale*, 2021, **13**, 5497–5506.

8 J. Lu, E. Choi, F. Tamanoi and J. I. Zink, *Small*, 2008, **4**, 421–426.

9 S. Angelos, E. Choi, F. Vögtle, L. De Cola and J. I. Zink, *Journal of Physical Chemistry C*, 2007, **111**, 6589–6592.

10 T. Fujino, S. Y. Arzhantsev and T. Tahara, *J Phys Chem A*, 2001, **105**, 8123–8129.

11 C.-W. Chang, Y.-C. Lu, T.-T. Wang and E. W.-G. Diau, *J Am Chem Soc*, 2004, **126**, 10109–10118.

12 D. Bandara and S. Burdette, *Chem Soc Rev*, 2012, **41**, 1809–1825.

13 C. Sah, A. Mahadevan, P. Kumar and S. Venkataramani, *Physical Chemistry Chemical Physics*, 2022, **24**, 7848–7855.

14 H. Satzger, C. Root and M. Braun, *Journal of Physical Chemistry A*, 2004, **108**, 6265–6271.

15 T. Fujino and T. Tahara, *J Phys Chem A*, 2000, **104**, 4203–4210.

16 T. Fujino, S. Y. Arzhantsev and T. Tahara, *Journal of Physical Chemistry A*, 2001, **105**, 8123–8129.

17 M. M. Sartin, M. Osawa, S. Takeuchi and T. Tahara, *Chemical Communications*, 2022, **58**, 961–964.

18 J. Wang, H. B. Liu and C. S. Ha, *Tetrahedron*, 2009, **65**, 9686–9689.

19 E. W. G. Diau, *Journal of Physical Chemistry A*, 2004, **108**, 950–956.

20 C. M. Stuart, R. R. Frontiera and R. A. Mathies, *Journal of Physical Chemistry A*, 2007, 111, 12072–12080.

21 Y. Kim, J. A. Phillips, H. Liu, H. Kang and W. Tan, *Proc Natl Acad Sci U S A*, 2009, 106, 6489–6494.

22 H. Rau and E. Lüddecke, *J Am Chem Soc*, 1982, **104**, 1616–1620.

23 L. Blancafort, **15**, 3166–3181.

24 I. K. Lednev, T.-Q. Ye, P. Matousek, M. Towrie, P. Foggi, F. V. R. Neuwahl, S. Umapathy, R. E. Hester and J. N. Moore, *Chem Phys Lett*, 1998, **290**, 68–74.

25 H. Rau, *Journal of Photochemistry*, 1984, **26**, 221–225.

26 C. J. Otolski, A. Mohan Raj, V. Ramamurthy and C. G. Elles, *Journal of Physical Chemistry Letters*, 2019, **10**, 121–127.

27 C. J. Otolski, A. M. Raj, V. Ramamurthy and C. G. Elles, *Chem Sci*, 2020, **11**, 9513–9523.

28 C. Slavov, C. Yang, L. Schweighauser, C. Boumrifak, A. Dreuw, H. A. Wegner and J. Wachtveitl, *Physical Chemistry Chemical Physics*, 2016, **18**, 14795–14804.

29 M. M. Sartin, M. Osawa, S. Takeuchi and T. Tahara, *Chemical Communications*, 2022, **58**, 961–964.

30 M. Dowds, D. Bank, J. Strueben, D. P. Soto, F. D. Sönnichsen, F. Renth, F. Temps and A. Staubitz, *J Mater Chem C Mater*, 2020, **8**, 1835–1845.

31 A. R. Ibrahim, M. F. Khyasudeen, J. Husband, S. M. Alauddin, N. F. K. Aripin, T. S. Velayutham, A. Martinez-Felipe and O. K. Abou-Zied, *Journal of Physical Chemistry C*, 2021, **125**, 22472–22482.

32 C. Bronner and O. S. Wenger, *Inorg Chem*, 2012, **51**, 8275–8283.

33 O. S. Wenger, *Chemistry - A European Journal*, 2011, **17**, 11692–11702.

34 P. Dongare, A. G. Bonn, S. Maji and L. Hammarström, *Journal of Physical Chemistry C*, 2017, **121**, 12569–12576.

35 S. M. Martin, A. N. Oldacre, C. A. Pointer, T. Huang, G. M. Repa, L. A. Fredin and E. R. Young, *Dalton Transactions*, 2021, **50**, 7265–7276.

36 X. Su and I. Aprahamian, *Org Lett*, 2011, **13**, 30–33.

37 X. Su and I. Aprahamian, *Org Lett*, 2013, **15**, 5952–5955.

38 J.-M. Saveánt and C. C. Tard, *J. Am. Chem. Soc*, 2014, **136**, 8910.

39 S. M. Martin, Z. J. Knepp, I. A. Thongchai, K. Englehart, K. Sorto, A. Jaffer, L. A. Fredin and E. R. Young, *New Journal of Chemistry*, 2023, **47**, 11882–11889.

40 J. L. Sadler and A. J. Bard, *J Am Chem Soc*, 1968, **90**, 1979–1989.

41 J. L. Sadler and A. J. Bard, *J Am Chem Soc*, 1968, **90**, 1979–1989.

42 J.-M. Savéant and C. Tard, *J Am Chem Soc*, 2014, **136**, 8907–8910.

43 A. N. Oldacre and E. R. Young, *RSC Adv*, 2020, **10**, 14804–14811.

44 R. C. Hamburger, T. Huang, S. M. Martin, C. A. Pointer, L. A. Fredin and E. R. Young, *Physical Chemistry Chemical Physics*, , DOI:10.1039/d3cp01211e.

45 K. A. Connors, *Binding Constants: The Measurement of Molecular Complex Stability*, John Wiley & Sons, Inc., New York, NY, 1897.

46 A. Kütt, T. Rodima, J. Saame, E. Raamat, V. Mäemets, I. Kaljurand, I. A. Koppel, R. Y. Garlyauskayte, Y. L. Yagupolskii, L. M. Yagupolskii, E. Bernhardt, H. Willner and I. Leito, *Journal of Organic Chemistry*, 2011, **76**, 391–395.

47 M. J. Frisch, G. W. Trucks, H. B. Schlegel, G. E. Scuseria, M. A. Robb, J. R. Cheeseman, G. Scalmani, V. Barone, G. A. Petersson, H. Nakatsuji, X. Li, M. Caricato, A. V. Marenich, J. Bloino, B. G. Janesko, R. Gomperts, B. Mennucci, H. P. Hratchian, J. V. Ortiz, A. F. Izmaylov, J. L. Sonnenberg, D. Williams-Young, F. Ding, F. Lipparini, F. Egidi, J. Goings, B. Peng, A. Petrone, T. Henderson, D. Ranasinghe, V. G. Zakrzewski, J. Gao, N. Rega, G. Zheng, W. Liang, M. Hada, M. Ehara, K. Toyota, R. Fukuda, J. Hasegawa, M. Ishida, T. Nakajima, Y. Honda, O. Kitao, H. Nakai, T. Vreven, K. Throssell, Jr. J. A. Montgomery, J. E. Peralta, F. Ogliaro, M. J. Bearpark, J. J. Heyd, E. N. Brothers, K. N. Kudin, V. N. Staroverov, T. A. Keith, R. Kobayashi, J. Normand, K. Raghavachari, A. P. Rendell,

J. C. Burant, S. S. Iyengar, J. Tomasi, M. Cossi, J. M. Millam, M. Klene, C. Adamo, R. Cammi, J. W. Ochterski, R. L. Martin, K. Morokuma, O. Farkas, J. B. Foresman and D. J. Fox, 2016, Gaussian 16, Gaussian, Inc., Wallingford CT.

48 R. Ditchfield, W. J. Hehre and J. A. Pople, *J Chem Phys*, 1971, **54**, 724–728.

49 M. M. Francl, W. J. Pietro, W. J. Hehre, J. S. Binkley, M. S. Gordon, D. J. DeFrees and J. A. Pople, *J Chem Phys*, 1982, **77**, 3654–3665.

50 W. J. Hehre, R. Ditchfield and J. A. Pople, *J Chem Phys*, 1972, **56**, 2257–2261.

51 P. C. Hariharan and J. A. Pople, *Theor Chim Acta*, 1973, **28**, 213–222.

52 A. D. Becke, *J Chem Phys*, 1993, **98**, 5648–5652.

53 C. Lee, W. Yang and R. G. Parr, *Phys Rev B*, 1988, **37**, 785–789.

54 S. H. Vosko, L. Wilk and M. Nusair, *Can J Phys*, 1980, **58**, 1200–1211.

55 P. J. Stephens, F. J. Devlin, C. F. Chabalowski and M. J. Frisch, *Journal of Physical Chemistry*, 1994, **98**, 11623–11627.

56 F. Weigend, M. Häser, H. Patzelt and R. Ahlrichs, *Chem Phys Lett*, 1998, **294**, 143–152.

57 C. Hansch, A. Leo and R. W. Taft, *Chem Rev*, 1991, **91**, 165–195.

58 C. J. Otolski, A. Mohan Raj, V. Ramamurthy and C. G. Elles, *Journal of Physical Chemistry Letters*, 2019, **10**, 121–127.

59 C. J. Otolski, A. M. Raj, V. Ramamurthy and C. G. Elles, *Chem Sci*, 2020, **11**, 9513–9523.

60 C. Slavov, C. Yang, L. Schweighauser, C. Boumrifak, A. Dreuw, H. A. Wegner and J. Wachtveitl, *Phys Chem Chem Phys*, 2016, **18**, 14795–14804.